On the Unique Structural Organization of the *Saccharomyces cerevisiae* Pyruvate Dehydrogenase Complex*

James K. Stoops‡§, R. Holland Cheng¶‖, Mohammed A. Yazdi**, Cheol-Young Maeng**, John P. Schroeter‡, Uwe Klueppelberg‡ ‡‡, Steven J. Kolodziej‡, Timothy S. Baker¶, and Lester J. Reed**

*From the ‡Department of Pathology and Laboratory Medicine, The University of Texas Health Science Center, Houston, Texas 77030, the ¶Department of Biological Sciences, Purdue University, West Lafayette, Indiana 47907, and the **Biochemical Institute and Department of Chemistry and Biochemistry, The University of Texas, Austin, Texas 78712*

Dihydrolipoamide acyltransferase (E_2), a catalytic and structural component of the three functional classes of multienzyme complexes that catalyze the oxidative decarboxylation of α-keto acids, forms the central core to which the other components attach. We have determined the structures of the truncated 60-mer core dihydrolipoamide acetyltransferase (tE_2) of the *Saccharomyces cerevisiae* pyruvate dehydrogenase complex and complexes of the tE_2 core associated with a truncated binding protein (tBP), intact binding protein (BP), and the BP associated with its dihydrolipoamide dehydrogenase ($BP \cdot E_3$). The tE_2 core is a pentagonal dodecahedron consisting of 20 cone-shaped trimers interconnected by 30 bridges. Previous studies have given rise to the generally accepted belief that the other components are bound on the outside of the E_2 scaffold. However, this investigation shows that the 12 large openings in the tE_2 core permit the entrance of tBP, BP, and $BP \cdot E_3$ into a large central cavity where the BP component apparently binds near the tip of the tE_2 trimer. The bone-shaped E_3 molecule is anchored inside the central cavity through its interaction with BP. One end of E_3 has its catalytic site within the surface of the scaffold for interaction with other external catalytic domains. Though tE_2 has 60 potential binding sites, it binds only about 30 copies of tBP, 15 of BP, and 12 of $BP \cdot E_3$. Thus, E_2 is unusual in that the stoichiometry and arrangement of the tBP, BP, and $E_3 \cdot BP$ components are determined by the geometric constraints of the underlying scaffold.

Pyruvate dehydrogenase complexes (PDCs)[1] are among the largest ($M_r \sim 10^6$-10^7) and most complex multienzyme structures known. They consist of a central core that has both functional and structural roles in organizing the complex, the dihydrolipoamide acetyltransferase (E_2) subunits associate to form the core complex that also serves as a scaffold to which the other components are attached (1–4). Electron microscopy (5–8) and x-ray crystallography (9–11) studies have revealed two fundamental morphologies of the E_2 cores. The cubic E_2 core of the *Escherichia coli* PDC has 24 subunits arranged with octahedral symmetry, whereas the pentagonal dodecahedral E_2 core of the PDC complexes from eukaryotes and some Gram-positive bacteria has 60 subunits arranged with icosahedral symmetry. The subunits form cone-shaped trimers at each of the 8 and 20 vertices of the cubic and dodecahedral structures, respectively. These trimers are interconnected by bridges to form a cage-like complex (8–11).

The E_2 subunit is a multidomain structure to which the other constituents of the functional PDC (1–4) bind (see Fig. 1). These include the pyruvate dehydrogenase (E_1) and dihydrolipoamide dehydrogenase (E_3). E_3 requires a binding protein (BP) to anchor it to the core of the yeast (12) and mammalian PDCs (13–15) though, in *E. coli* and *Bacillus stearothermophilus* PDCs, BP is not required (1–4).

It is widely held that the constituent proteins are bound to the outer surface of the E_2 cores though there is no consensus concerning the sites of binding (1–4). Radial mass analysis of scanning transmission electron micrographs of *E. coli* PDC and its subcomplexes supports a model whereby E_1 and E_3 are arranged on the edges and faces of the cubic structure, respectively (16, 17). Conversely, cryo-electron microscopy (cryoEM) studies of frozen hydrated samples of $E_1 \cdot E_2$ and $E_3 \cdot E_2$ subcomplexes of *E. coli* PDC suggested that E_1 and E_3 are tethered to the core by flexible binding domains and thus do not occupy fixed positions with respect to the cubic core (6). Comparable studies of the mammalian pentagonal dodecahedron-like subcomplexes of PDC again led to similar conclusions about the localization of E_1 and E_3 since their radial positions appeared to vary, leaving a 0–40 Å gap between them and the core. Thus, it was proposed that these constituents are attached to the cores by extended, flexible tethers (7).

There is no direct evidence concerning the localization of BP molecules on the yeast and mammalian E_2s. Because the yeast E_2 binds about 12 $BP \cdot E_3$ molecules, it was proposed that one $BP \cdot E_3$ binds to each of the 12 faces of the core structure (12).

No studies have implicated a structural role for the internal cavities of the cubic or pentagonal dodecahedral PDCs in binding or organizing the constituent proteins. Our three-dimensional reconstructions of the *Saccharomyces cerevisiae* truncated E_2 core (tE_2) and its complexes with truncated BP (tBP), BP, and $BP \cdot E_3$ show that the central cavity indeed directly affects the organization and extent of binding of these constituents to the core.

[1] The abbreviations used are: PDC, pyruvate dehydrogenase complex; E_1, pyruvate dehydrogenase; E_2, dihydrolipoamide acetyltransferase; E_3, dihydrolipoamide dehydrogenase; tE_2, truncated dihydrolipoamide acetyltransferase; BP, binding protein; tBP, truncated binding protein; cryoEM, cryo-electron microscopy.

EXPERIMENTAL PROCEDURES

Protein Preparations—The *S. cerevisiae* genes or subgenes encoding tE$_2$, tBP, BP, and E$_3$ were expressed in *E. coli*, and the recombinant proteins were purified to homogeneity as described (12, 18). The tE$_2$ subunit (residues 206–454) had Ser-Gly at the N terminus. The tE$_2$ subunit (residues 181–454) and tBP (residues 206–380) had His$_6$-Gly-Ser at the N terminus to facilitate purification. Monomeric BP binds an E$_3$ homodimer (12). Solutions of the individual proteins in 25 mM potassium phosphate buffer, pH 7.3, were mixed to the appropriate ratios, and the mixtures were diluted to a protein concentration of 0.1 mg/ml prior to electron microscopy. tE$_2$ (residues 206–454) and BP were mixed in a molar ratio of 1:24; BP was added to tE$_2$ (residues 206–454) and then E$_3$ was added (molar ratio 1:12:12); and tE$_2$ (residues 181–454) and tBP were mixed in a molar ratio of 1:30. The same preparations of tE$_2$, BP, and E$_3$ used to determine the binding stoichiometries were used to prepare samples for electron microscopy.

Electron Microscopy—A 3-μl sample of the preparations (0.1 mg/ml) was deposited, blotted, and quick-frozen in liquid ethane on a glow-discharged carbon-coated holey grid. The vitrified samples were recorded at ~1 μm underfocus at ~9 e/Å^2 dose for image processing except for the tE$_2$·tBP preparation, which was recorded at an underfocus of 0.5 μm. A second exposure at 1.7 μm underfocus was recorded for display (see Fig. 2) and as an aid in analyzing the images. The images were recorded on Kodak SO 163 film at a nominal magnification × 50,000 in a JEOL JEM 1200 electron microscope operated at 100 kV.

Image Processing—The micrographs were digitized with an Eikonix 1412 digitizer at 5.7 Å/pixel. The micrographs selected for computer processing were chosen as described previously (8). Particle images were screened using a model-based approach (19). An initial three-dimensional reconstruction was obtained with common-lines and Fourier-Bessel procedures (20), and the resulting model was used for refinement (21). The reconstructions were further improved by correcting for magnification variations using only those images that were within 3% of the average size (22, 23). A set of 51, 42, 29, and 42 particle images were selected to compute at 20 Å resolution (21) the final three-dimensional reconstructions of tE$_2$, tE$_2$·tBP, tE$_2$·BP, and tE$_2$·BP·E$_3$, respectively. Complete icosahedral symmetry was imposed on the final density maps (20), and they have been corrected for the contrast transfer function of the electron microscope (8) and filtered to the resolution limit.

Radial Density Scaling—The reconstructions were scaled using SUPRIM (24) so that a semi-quantitative comparison could be made between their radial density plots. This was accomplished by applying a threshold to the tE$_2$ reconstruction so that its volume corresponded to its molecular weight. The average pixel value in a radial shell (r = 150–156 Å) outside the structure was subtracted from each pixel in the reconstruction of the complexes. Then each pixel in the three complexes was multiplied by that factor which matched the average pixel value inside the cone portion of its scaffold to that for the tE$_2$ reconstruction. The interior portion of the cone was deemed most appropriate for the scaling since the bridges and the base portion of the trimers undergo conformational change upon binding of the constituents to the core (see "Three-dimensional Reconstructions").

The scaled radial density function for the computer simulation of tE$_2$·BP·E$_3$ was determined by filtering the E$_3$ x-ray structure (25) to 20 Å and thresholding it to its molecular weight with pixels outside the molecule set to 0. Then the electron density map of E$_3$ was multiplied by a value that matched the average density of E$_3$ to the average density of the bone-shaped object on the 5-fold axis of tE$_2$·BP·E$_3$. The corrected E$_3$ was then added to the corrected tE$_2$·BP reconstruction in the optimum position (see below).

Computer Simulation and Optimization—The x-ray structure of *Azotobacter vinelandii* E$_3$ (25) (obtained from the Protein Data Bank, Brookhaven National Laboratory, code 3LAD (26)) was used in the computer simulation. A lower resolution x-ray structure of the yeast E$_3$ (27) is similar to that of *A. vinelandii* but not on deposit. The E$_3$ structure was low-pass filtered to the 20 Å resolution of the reconstructions, and 12 were docked in corresponding positions in or near the pentagonal openings of the tE$_2$·BP core. Icosahedral symmetry was imposed by rotation of the structure about each of the symmetry axes of an icosahedron. Since symmetrization requires a large number of rotations, the effect of aliasing-induced artifacts was assessed by comparing the tE$_2$·BP reconstruction before and after rotational symmetrization. With the molecules interpolated to a 110 × 110 × 110 pixel volume, the comparisons agree to less than 10 Å as determined by the calculation of the phase residual (28) in a spherical shell.

Newton's method employing discrete approximation (29) was used to optimize the correlation coefficient (30) between the symmetrized

Physicochemical characteristics of the tE₂ scaffold and its components

The organization of the domains and the positions of truncation for E$_2$ and BP are shown in Fig. 1.

Proteins	Mr of protein	~mol bound[a]/mol core	Mr of complex
tE$_2$	26,991		1,619,460
tBP[b]	19,641	30	2,403,510
BP	42,052	15	2,250,240
E$_3$	103,116		
BP · E$_3$	145,168	12	3,361,476

[a] The stoichiometry of binding was determined as described (12, 18).
[b] The tE$_2$ consisted of residues 181–454, Mr = 30,238, in the tE$_2$ · tBP preparation.

tE$_2$·BP with 12 docked E$_3$s and the tE$_2$·BP·E$_3$ reconstruction by varying the position and orientation of the docked E$_3$ molecules. This method found several local maxima for the correlation coefficient, each of which gave a similar symmetrized structure. Starting structures for the optimization included those with the E$_3$ molecules docked in the 5-fold opening as well as those with E$_3$ outside the molecule and approximately tangent to its surface.

Display—The three-dimensional reconstructions were displayed as shaded solid surface models by SUPRIM (24), and the images were rendered by SYNU (31) using a Mitsubishi S3600–3OU dye sublimation color printer.

RESULTS AND DISCUSSION

CryoEM—Galleries of frozen hydrated samples of the 60-subunit tE$_2$ core (tE$_2$) and complexes formed with tBP (tE$_2$·tBP), BP (tE$_2$·BP), or BP·E$_3$ (tE$_2$·BP·E$_3$) show particles that appear similar irrespective of their composition, and they all exhibit the 5-, 3-, 2-fold symmetries characteristic of a pentagonal dodecahedron structure (Fig. 2).

The molecular weight of each complex, and its components and the stoichiometries of the components are summarized in Table I. Interestingly, though the tE$_2$·BP·E$_3$ mass is nearly double that of tE$_2$, the particles appear nearly identical in size (*cf*. tE$_2$ and tE$_2$·BP·E$_3$ images in Fig. 2). This contrasts with the reported change in the size of the mammalian pentagonal dodecahedral E$_2$·BP·K complex that occurs with the addition of E$_3$ (K denotes bound kinase). It was proposed that there is a 0–40 Å gap between the outer surface of the E$_2$·BP·K and E$_3$ (7). The apparent discrepancy between these two studies may be related to differences in the composition of the complexes. The tE$_2$ core lacks the flexible lipoyl and E$_1$-binding domains (residues 1–205) and the kinase. The binding of E$_3$ to the core produces a conformational change in the scaffold (see below) that could alter the disposition of the lipoyl and E$_1$-binding domains of E$_2$ or the kinase on the scaffold, possibly making the observed change upon addition of E$_3$ ambiguous. Furthermore, direct comparisons of noisy particle images are inconclusive. Therefore, three-dimensional reconstructions of these molecules have been computed and analyzed. We have utilized the truncated E$_2$ core since it eliminates any ambiguity resulting from the flexibility of the N-terminal lipoyl and E$_1$-binding domains (Fig. 1). The tE$_2$ exhibited catalytic activity similar to that of the wild-type E$_2$ (12).

Three-dimensional Reconstructions—The icosahedral particle reconstruction techniques used to compute the structures (Fig. 3) make it possible to visualize the disposition of the constituents in three dimensions. However, the apparent morphology of the constituents is influenced by the icosahedral symmetry imposed on the reconstruction. This is because the bound constituents are not present in 60 copies, and they are apparently not disposed with icosahedral symmetry. Even so, it is possible to obtain insight into the gross shape of the components (see below, computer simulations).

As suggested by the cryoEM images (Fig. 2), all the structures have approximately the same size, 230 Å in diameter as

measured along the 3-fold axis (Fig. 3). The tE$_2$ structure (residues 221–454) has 12 large openings ~63 Å in diameter on the five-fold axes that lead into a large central cavity of ~76–140 Å in diameter. The molecule consists of 20 cone-shaped trimers on the 3-fold axes that are interconnected by 30 bridges on the 2-fold axes. The tip of the cone-shaped trimer is directed toward the center of the structure and measures ~60 Å from its triangular shaped base on the outside surface.

The tBP, BP, and BP·E$_3$ components are centered on the 12 pentagonal faces of tE$_2$ (Fig. 3). The tBPs have a bowling pin morphology whose base protrudes ~25 Å outside of the tE$_2$ face, whereas the spherical BP is located near the center of the structure ~90 Å from the outside surface. The pentagonal-shaped BP·E$_3$ nearly fills the pentagonal opening on each face, thereby obscuring internal features. The corners of the pentagon show connectivity near the vertices of the five adjacent trimers on the outside surface of the scaffold. The illusion that tBP (half the molecular weight of BP) appears so much larger than BP is contributed to by two factors: (i) ~2 times more tBPs than BP are bound to tE$_2$, and (ii) more of the tBP than BP is located near the five-fold axis of the complex, so a larger portion of the BP protein density smears out due to the icosahedral averaging process (see below).

Previous studies and interpretative models of the PDCs have suggested that the constituent proteins are bound to the out-side of the E$_2$ scaffold (1–4). A pertinent example is the *B. stearothermophilus* PDC that also has a pentagonal dodecahedral core. It was proposed that the N-terminal portion of E$_2$ with either E$_1$ or E$_3$ attached extends outward from its core (32). It was surprising then to find in the case of *S. cerevisiae* PDC, that major portions of tBP, BP, and BP·E$_3$ lie inside the tE$_2$ core. The dispositions of these components are revealed in cut-away representations of the three-dimensional density maps (Fig. 4). The large cavern-like space into which the 20 cone-shaped trimers extend is apparent in the tE$_2$ reconstruction (Fig. 4). At the threshold chosen to represent the structures of the complexes, the tBP bowling pins and the BP spheres do not contact the inner wall of the scaffold. The parts of these proteins visualized in the reconstructions are near the five-fold axis of the core, and their innermost portions are ~100 Å from the outer surface of the complex. In these images, the volume surrounding the cone of the trimer is occupied with protein, and thus obscures this feature. BP·E$_3$ has a mushroom shape that extends ~100 Å toward the center of the scaffold but shows no connection to its inside.

It appears that the portion of tE$_2$ that forms the bridge between trimers undergoes a conformational change upon binding the constituents. The bridge thickens after tBP or BP binds to tE$_2$ but thins when BP·E$_3$ is present (Fig. 4). In addition, the shape of the base of the trimer changes markedly (Fig. 3). A comparison of serial slices cut through the bridges, starting from the outside of the structure in a two-fold orientation (Fig. 5), further supports this proposal. Binding of tBP, BP, and BP·E$_3$ results in a change in the protein distribution in the bridge, and this is most pronounced in the tE$_2$·BP·E$_3$ complex. In this latter instance, the size and intensity (*i.e.* connectivity) of the bridges is greatly reduced. Such large conformational changes make it impossible to carefully decipher the disposition of the constituents and their sites of interaction with the scaffold by means of difference map analysis, which requires significant portions of the compared structures to be equivalent.

As a consequence, we have utilized a variable threshold approach to help visualize the structural features inside each complex. The conventional approach of choosing a threshold value (contour level) that gives a volume that corresponds to the molecular weight of tE$_2$ was employed in generating the views of the reconstructions shown in Figs. 3 and 4. To facilitate comparisons of the scaffold structures in the different complexes, a threshold was applied to each complex to render

FIG. 1. **Diagrammatic representation of the structural domains of *S. cerevisiae* E$_2$ core and BP.** The domains are connected by flexible *linkers*. The *arrows* denote the approximate position of truncation of the subunits used in this investigation (see Table I). The binding domain for BP resides in the C-terminal (catalytic) half of E$_2$ (residues 221–454).
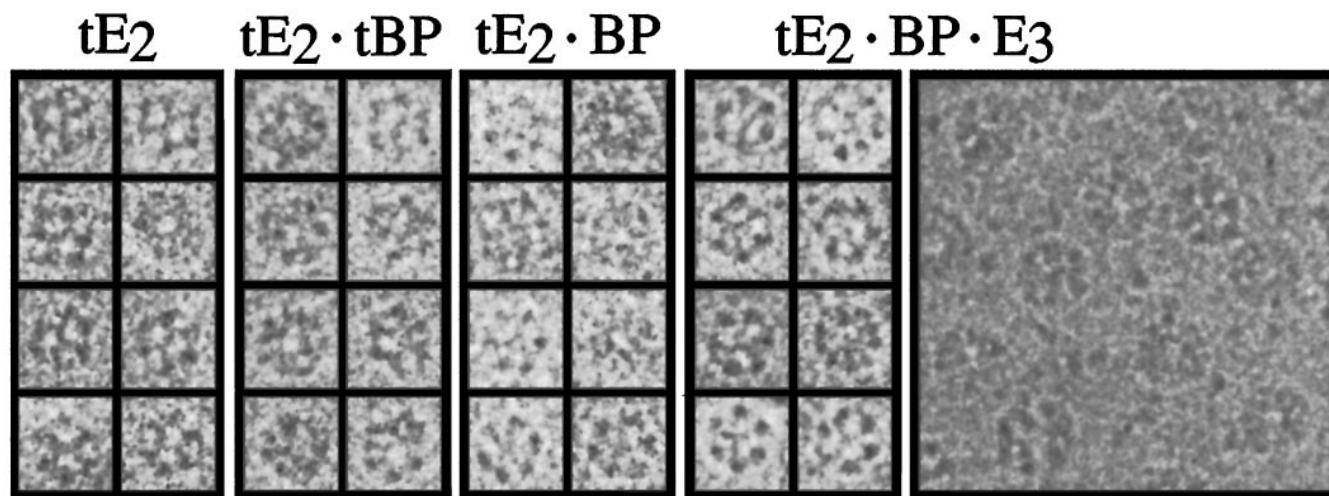
FIG. 2. **Galleries of images of frozen-hydrated tE$_2$ complexes.** The different complexes appear similar and exhibit the characteristic pentagonal dodecahedron morphology. The electron microscopy field of tE$_2$·BP·E$_3$ indicates that the BP·E$_3$ components do not reside tethered outside of the core. For an opposing interpretation, see text. The *scale bar* in this and subsequent figures corresponds to 100 Å.
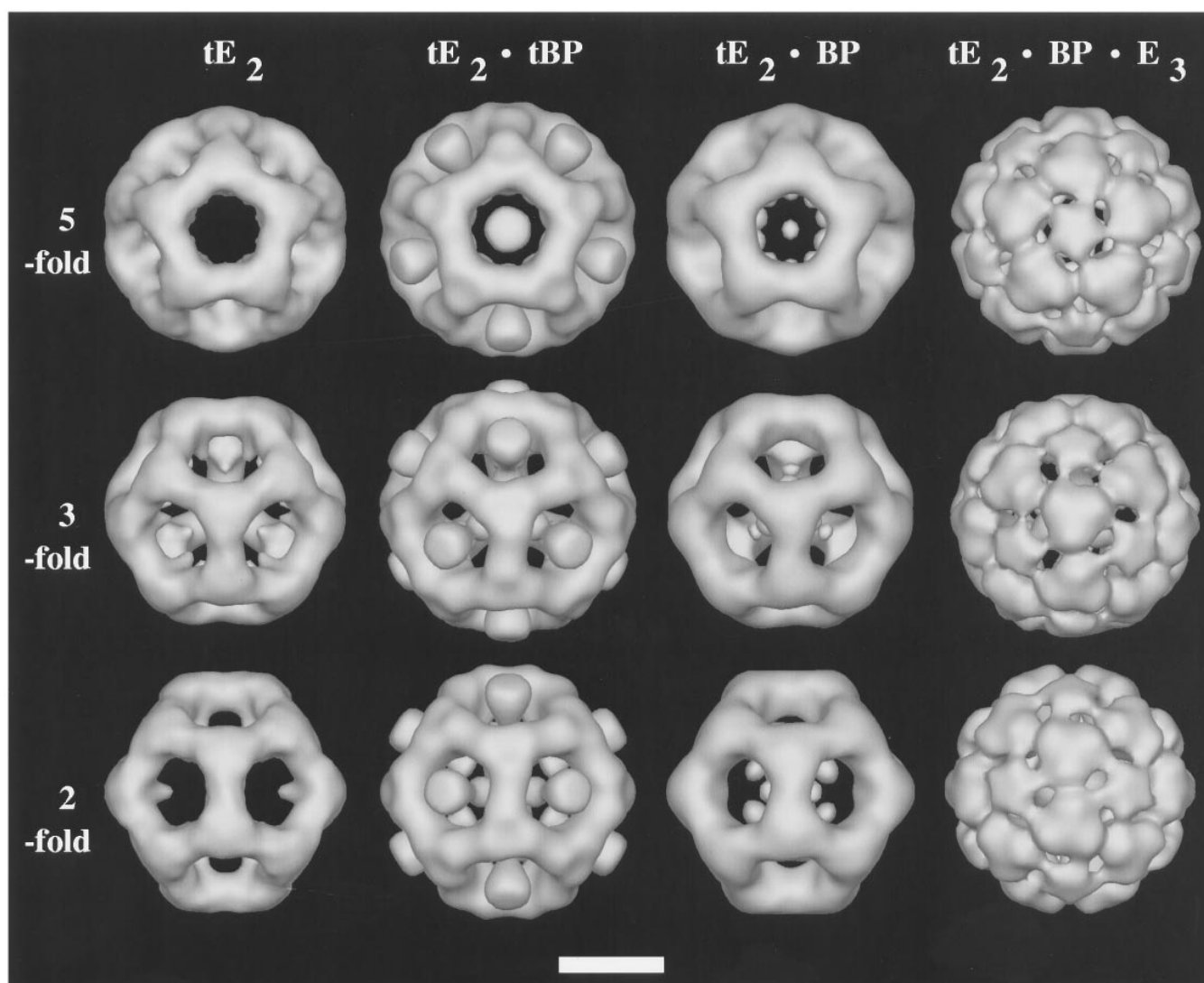
FIG. 3. **Surface shaded representations viewed along 5-, 3-, and 2-fold axes of symmetry of three-dimensional reconstructions of the tE₂ complexes.** The tBP, BP, and BP·E₃ components are centered on the 12 pentagonal faces of the tE₂ core.
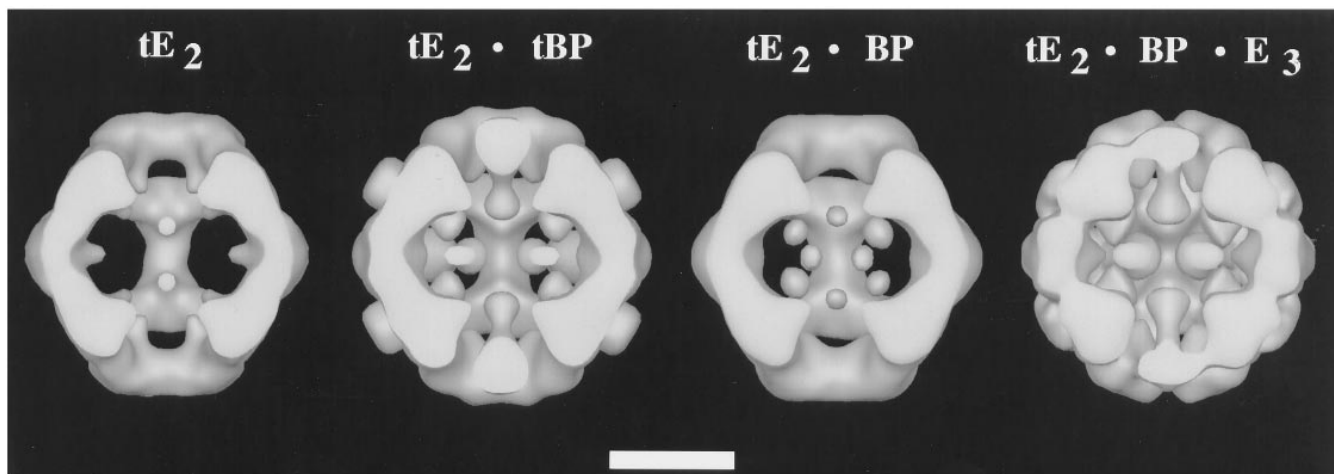
FIG. 4. **Reconstructions viewed along the 2-fold axis with the closest half removed to reveal internal details.** Surprisingly, most of the constituent proteins reside inside the tE₂ cage.

the scaffolds similar to each other. This process necessarily underestimates the volumes of tBP, BP, and BP·E₃ because each of these is present in fewer than 60 copies, and the density of each is significantly down weighted due to the icosahedral averaging. This, in turn, has resulted in loss of significant information regarding the interaction of the components with the core (see below) and accounts for the apparent lack of attachment of the components with the internal scaffold shown in Figs. 3 and 4.
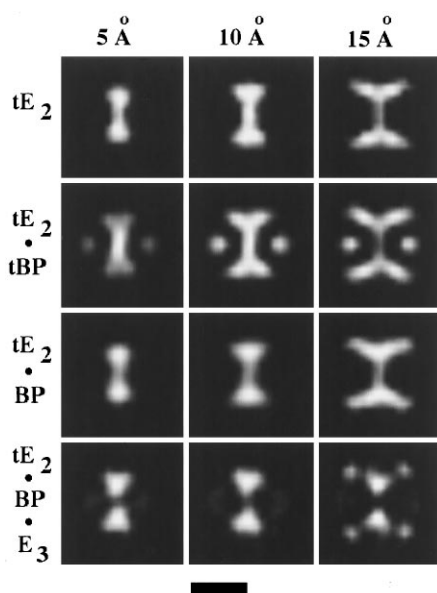
FIG. 5. **Galleries of protein distribution in 5 Å thick slices cut normal to the 2-fold face of the complexes at the indicated depth from the surface.** The comparisons show that the protein distribution is altered in the bridges and the base of the tE$_2$ trimers upon binding of the constituents (conformational change).

tBP, BP, and BP·E3 Morphologies and Interactions with the Core—Accordingly, we have investigated the effect of lowering the threshold on the morphology of the scaffold and its bound constituents. Figs. 6 and 7 show cut-away views of the reconstructions rendered at threshold values that portray connections between the tBP, BP, and BP·E$_3$ constituents and the scaffold, thus making it possible to locate their likely binding site (see below). These threshold levels result in about 2-fold over-estimate of the molecular weight of each structure because of the increased volume of the core. With the exception of BP, at lower thresholds, the shapes of the protein components are not appreciably affected, indicating that most of tBP and BP·E$_3$ density must lie near the icosahedral 5-fold axis. However, the BP protein is positioned away from the symmetry axis, and the large increase in its apparent size is attributed to the use of the low threshold (*cf.* Figs. 4 and 6).

At reduced threshold, a bulbous mass connected through a narrow neck appears at the tip of the cone-shaped trimer in the tE$_2$ core (*cf.* Figs. 4 and 6). This feature extends the internal structure of tE$_2$ to ~90 Å from the outside of the core. The radial density plot of tE$_2$ is consistent with the presence of this additional protein with a peak at ~25 Å (Fig. 8). It should be noted that the pentagonal openings that form channels to the center of the molecule persist at the low threshold levels (*cf.* Figs. 4 and 6).

BP consists of an N-terminal lipoyl domain, an E$_3$-binding domain, and a C-terminal domain that binds tE$_2$. These domains are held together by flexible tethers (Fig. 1). tBP, which lacks the lipoyl and E$_3$-binding domains, contacts the tE$_2$ trimer, possibly by interacting with the bulbous, low density feature associated with its tip (Fig. 6). The protein density extends ~100 Å from the inner end of tE$_2$ to ~25 Å beyond the outside surface of the scaffold near the 5-fold axis. Given the stoichiometry of ~30 tBP bound per tE$_2$·tBP complex (18), each bowling pin-shaped feature is presumably comprised, on average, of ~2.5 tBP subunits. Though the true morphology of tBP is not reliably represented in the reconstructions because of the enforced icosahedral symmetry, it is still possible to conclude that the tBP molecules form an extended structure of ~100–125 Å in length. The extended shape of tBP may be influenced by the internal "environment" of the core (Fig. 6).

It was somewhat surprising to find that the BP, which has twice the molecular weight of tBP (Table I), appears as a condensed sphere ~70 Å inside the tE$_2$ core (Fig. 6). As mentioned above, most of the BP protein apparently deviates from the icosahedral symmetry of the core. The BP molecules also make contact near the inner tip of the tE$_2$ trimer, again consistent with an assignment placing the binding site for BP near the inner tip of tE$_2$ (Fig. 6). The more highly condensed distribution of BP in the cavity could explain the ~2-fold decrease in its binding to tE$_2$ compared with tBP (12, 18). Apparently, more copies of the extended tBP structure may access binding sites inside the core. Because the E$_3$ homodimer forms a 1:1 association with BP (12), whatever limits BP binding would correspondingly limit the amount of E$_3$ that can bind to tE$_2$ (Table I).

The different distributions of tBP and BP (Fig. 6) suggest that the N-terminal residues (1–217) have an important role in determining how BP binds to the scaffold. This N-terminal region could keep BP in a more condensed form, thereby fixing its E$_3$-binding site so that E$_3$ becomes anchored near the center of the scaffold. Even though the BP protein appears more condensed than tBP, the radial density plot of the non-thresholded reconstruction shows (like tBP) that some of its protein extends into the outer shell of the scaffold (see below).

The similar morphologies of tBP and BP·E$_3$ in the complexes (Figs. 6 and 7) may partially arise due to the symmetrization enforced in the icosahedral reconstruction process. Significant differences do exist however. For example, the tBP bowling pins make minimal contacts with the outer surface of the tE$_2$ core, whereas the BP·E$_3$ "mushroom" makes extensive contacts at the outer pentagonal face of the tE$_2$ scaffold. Furthermore, BP·E$_3$ does not extend as far outside the core as does tBP (*cf.* tE$_2$·tBP and tE$_2$·BP·E$_3$ structures in Fig. 3).

BP·E$_3$ also contacts the inner tip of the cone-shaped tE$_2$ trimer, thus this location of the BP binding site is consistent in the three reconstructions (Figs. 6 and 7). BP only contacts the scaffold at the tip of the tE$_2$ trimer, whereas tBP and BP·E$_3$ also contact the pentagonal opening of the core at the reduced threshold (Figs. 6 and 7). This latter contact may merely be an incidental result of the "swelling" of the core, and the constituents at the lower threshold levels. It is unlikely that BP binds at the pentagonal openings since BP does not contact this region of the structure. Recall that tBP and BP·E$_3$ are connected to the tip of the tE$_2$ trimer through narrow extensions (Figs. 6 and 7) that are unlikely to be generated from a global expansion of the internal core at the lower threshold.

The E$_3$-binding domain of the E$_2$ component of the *B. stearothermophilus* PDC has recently been shown to bind near the 2-fold axis of E$_3$ (32). If the yeast E$_3$ has a similar location for its BP binding domain, it would be located near the center of the bone-shaped dimer inside the core. Computer simulations indicate that the tE$_2$·BP·E$_3$ reconstruction would not reveal this location (see below). Instead, a cut-open view of the tE$_2$·BP·E$_3$ structure (Fig. 7) shows protein connected to E$_3$ at its inner end. The opposite end of E$_3$, near the outside of the core, is framed by the pentagonal face of the core.

The radial density plots give a reliable estimation of the relative protein density distribution in the molecules (33). The tE$_2$ core has a density peak at a radius ~90 Å from the center of the molecule that corresponds to the outer shell of the scaffold (*cf.* Figs. 6 and 8). Smaller peaks at 25 and 50 Å are associated with the bulbous feature on the inner tip of the tE$_2$ trimer. The addition of BP to the core results in a significant increase in density at 35 Å with a valley at 60 Å (Fig. 8). This is consistent with the tE$_2$·BP reconstruction that shows a significant portion of the condensed BP located below the tip of the tE$_2$ trimer (Fig. 6). However, the increase in the peak at 90 Å
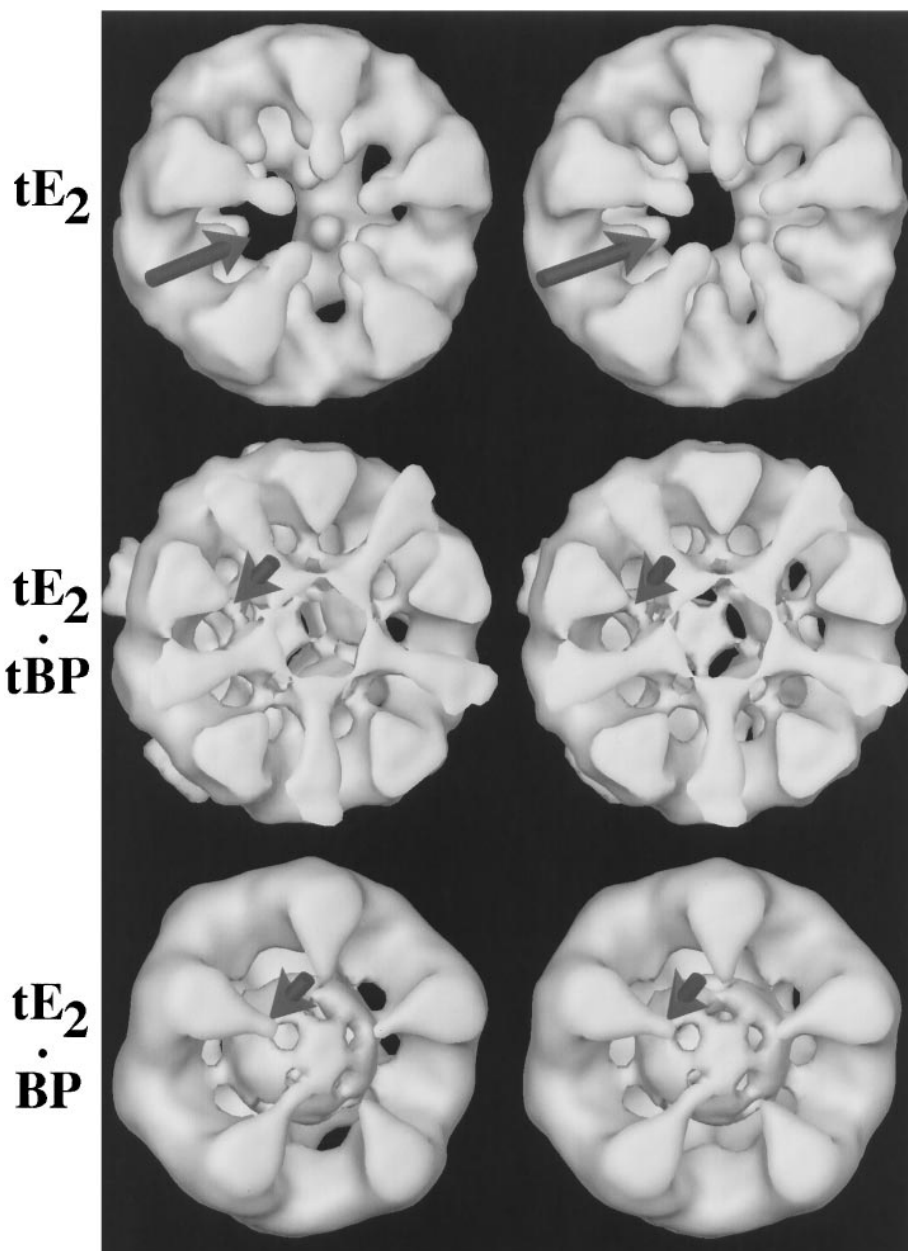
FIG. 6. **Stereo views along the five-fold axis of the cut-away reconstructions.** The structures are rendered at a lower threshold than that used in Figs. 3 and 4 to help locate the binding site of tBP and BP on the scaffold (*arrows*). The *arrow* in the tE_2 image denotes the channel below the pentagonal opening through which the tBP, BP, and BP·E_3 constituents enter the inside of the core. The BP binding site is near the inner tip of the cone-shaped trimer, and the BP protein is condensed near the center of the core where its E_3 binding site anchors E_3 (see Fig. 7).

upon addition of BP (Fig. 8) indicates that a portion of the BP protein extends into the outer shell. Perhaps the N-terminal lipoyl domain resides in this region of the scaffold and, because of its flexibility, is not seen in the reconstruction (Fig. 6). The addition of tBP to the core also results in a significant density at low radii (peak at 45 Å), and the valley in the radial density plot at 60 Å corresponds to the neck of the bowling pin-shaped tBP (Fig. 6). The addition of BP·E_3 to the core results in the largest increase in the inner density, which is consistent with its larger mass (Table I). Comparison of the tE_2·BP and tE_2·BP·E_3 radial density plots clearly shows that at least part of E_3 is located inside the scaffold (Fig. 7). Even though the components contribute to the density of the outer shell, they do not result in a significant increase in its radius, which is consistent with the similar size of the reconstructions (Fig. 3).

There appear to be smaller particles exterior to the core in the tE_2·BP·E_3 field (Fig. 2) that may be E_3. These may arise from incomplete binding of E_3 to the core, or some E_3 may be tethered to the core at random positions on the outside of its surface as

proposed by other investigators (6, 7) and a referee based on the interpretation of frozen-hydrated images. Because there is no apparent ring of particles around most of the core images and the radial density plot exhibits an increase in density inside the core upon E_3 binding, we favor the former interpretation.

Computer Simulations of E3 Binding—To assess the extent to which icosahedral averaging distorts and smears out density features in components that are not disposed with icosahedral symmetry on the core, we have imposed icosahedral symmetry on a model consisting of the tE_2·BP reconstruction (Fig. 9) to which 12 copies of the atomic structure of *A. vinelandii* E_3 (25) were docked in the pentagonal cavities. Newton's method (29) was used to optimize the correlation coefficient (30) between the simulation and the corresponding tE_2·BP·E_3 reconstruction (Fig. 9, *B* and *C*). The best matches corresponded to structures in which the E_3 was positioned off the 5-fold axis and touching the wall of the pentagonal opening (Fig. 9A). This position suggests the existence of an interaction that stabilizes E_3 against the wall of the core (Fig. 9A) and thereby reconciles the
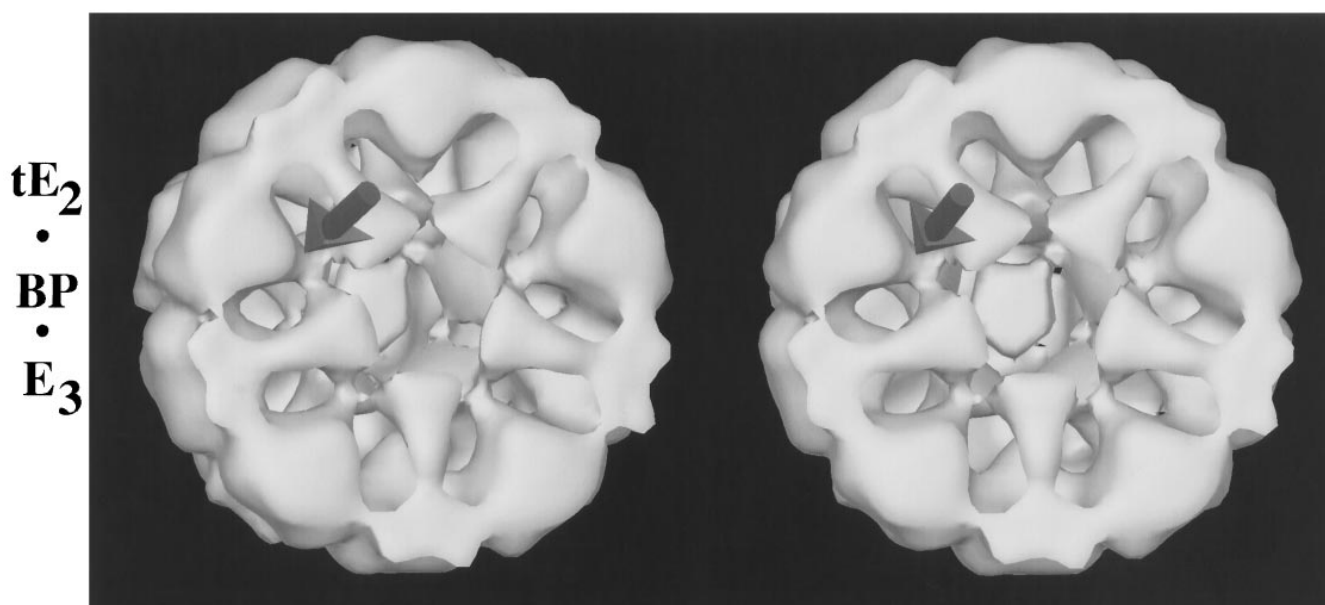
FIG. 7. **Stereo view of the cut-away structure viewed on the 5-fold axis.** The threshold is similar to the images in Fig. 6. The *arrow* denotes the binding site for the BP·E₃ component near the inner tip of the scaffold, which is presumably the BP binding site, *cf.* Fig. 6. Most of the E₃ dimer resides inside the core.

FIG. 8. **Radial density plots of tE₂ and its complexes.** The outer peak (~90 Å) corresponds primarily to the density in the outer shell of the tE₂ scaffold, and the inner peaks (35–45 Å) correspond primarily to the density ascribed to the components. This analysis corroborates the structural information in Figs. 6 and 7, which indicates most of the component proteins reside inside the tE₂ core. The reconstructions were not thresholded for this analysis. Radial density plots are in arbitrary units.
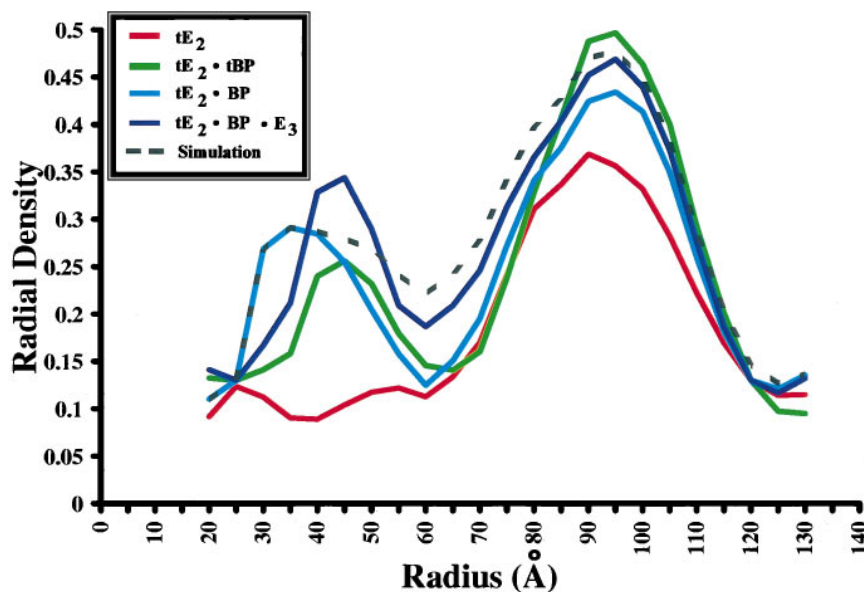
observed connectivity to the five adjacent trimers (Fig. 3, tE₂·BP·E₃). The corresponding radial density plot nicely matches to that of tE₂·BP·E₃ except at radii below 45 Å, thus corroborating the presence of E₃ inside the outer shell (Fig. 8). Any discrepancy below 45 Å may result from a minor structural change of the complex upon E₃ binding.

The bone-shaped E₃ (Fig. 9A) converts to a peg-shaped object with a knob on its interior end after symmetry averaging (Fig. 9B). The knob feature arises due to merging of the BP sphere with the end of the E₃ x-ray model, thus indicating that the bulb seen in the tE₂·BP·E₃ reconstruction (Fig. 9C) results from E₃ abutting a portion of the BP protein. A simulation computed without the BP component lacks the bulb on the end of E₃ (figure not shown). The larger size of the bulb in the reconstruction (*cf.* Fig. 9, *B* and *C*) suggests that the BP protein is located closer to the 5-fold axis in the tE₂·BP·E₃ structure compared with that in the tE₂·BP structure. This apparent join

of E₃ to BP may be related to its BP binding site. However, *B. stearothermophilus* E₃ has a site that binds it to the core near its center (32). Further resolution of this putative binding site in the reconstruction may not be possible because symmetry averaging results in a diminution of about half of the volume of E₃ (primarily the protein that lies off the 5-fold axis, *cf.* Figs. 9, *A* and *B*).

Structure-Function Relationships—In a model of the *A. vine-landii* tE₂·E₃ complex, the E₃ was positioned in the more conventional manner with the E₃ entirely on the outside of the scaffold (11). In this proposed arrangement, the major axis of E₃ lies approximately parallel to the outside face of the cubic core. However, a computer simulation with E₃ positioned in a comparable manner on the tE₂·BP reconstruction gave a radial density profile (data not shown) similar to tE₂·BP and yet failed to exhibit the increase in density between 45–90 Å as observed in the tE₂·BP·E₃ radial density plot (Fig. 8).

The crystal structure of the cubic truncated E₂ from *A. vine-*
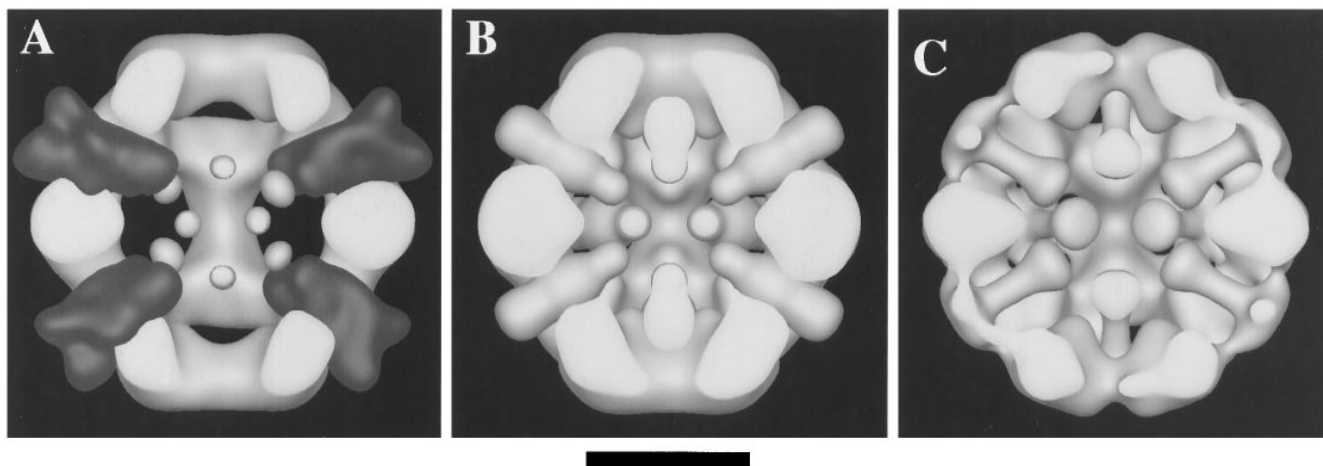
FIG. 9. **Computer-generated tE₂·BP·E₃ simulation compared with reconstructed tE₂·BP·E₃.** Twelve E₃ molecules (*shaded*, four shown) positioned in the cut-away scaffold so they touch the wall of the pentagonal opening of the tE₂·BP complex (*A*) give the best correlation coefficient when comparing the simulation (*B*) with the reconstruction of tE₂·BP·E₃ (*C*). Note that more of the density is cut away in these structures compared with those in Fig. 4 in order to reveal the E₃ interactions. Over 100 simulations were compared with the reconstruction, and many local maxima were found by the optimization technique. Each of the local maxima for the best visual fits resulted in a structure similar to that shown.

landii reveals that the catalytic residues and the CoA- and lipoamide-binding sites reside on the walls of a 29 Å long channel that traverses the interfaces of the subunit trimer (11). The crystal structure of the *A. vinelandii* E₃ shows that the isoalloxazine ring (the reactive component of FAD) is located in a cleft ~25 Å from either end of the bone-shaped dimer (25). Our three-dimensional reconstruction of tE₂·BP·E₃ shows one one end of E₃ located near the surface of the tE₂ core, thus its catalytic site and that of E₂ are located within the outer surface of the scaffold near the 5- and 3-fold axes, respectively. This structural organization has important consequences regarding the function of the PDC. The N-terminal lipoyl domain of E₂ ("swinging arm") (Fig. 1) that shuttles intermediates of catalysis between the active sites accomplishes this by moving down into the scaffold to access the E₂ and E₃ active sites. The other isoalloxazine ring of E₃ is located inside the scaffold ~75 Å from the outer surface and may not significantly participate in the catalysis.

Besides PDC, *Bacillus subtilis* riboflavin synthase has icosahedral symmetry and is the only multienzyme complex known to have the structure of an icosahedron. It consists of 60 β-subunits that enclose an α-trimer in its core. The crystal structure shows that the encapsulated α₃ does not maintain a fixed position within the core, and it was proposed that there is no discrete binding site for α inside the scaffold (34). Rather, the internal α₃ is encapsulated in a manner similar to the nucleic acid in nucleocapsids of virions.

For most protein oligomers like tE₂, the number of binding sites, the interactions between subunits, and subunit shape determine the architecture of the molecule. However, *S. cerevisiae* PDC is unusual in that the stoichiometry and arrangement of the tBP, BP, and E₃·BP components are determined also by the geometric constraints of the underlying scaffold. Of course, it is possible that other members of the α-keto acid dehydrogenase family also enjoy a similar structural organization.

REFERENCES

1. Perham, R. N. (1991) *Biochemistry* **30,** 8501–8512
2. Reed, L. J., and Hackert, M. L. (1990) *J. Biol. Chem.* **265,** 8971–8974
3. Guest, J. R., Angier, S. J., and Russell, G. C. (1989) *Ann. N. Y. Acad. Sci.* **574,** 76–99
4. Patel, M. S., and Roche, T. E. (1990) *FASEB J.* **4,** 3224–3233
5. Oliver, R. M., and Reed, L. J. (1982) in *Electron Microscopy of Proteins* (Harris., J. R., ed) Vol. 2, pp. 1–47, Academic Press, London
6. Wagenknecht, T., Grassucci, R., and Schaak, D. (1990) *J. Biol. Chem.* **265,** 22402–22408
7. Wagenknecht, T., Grassucci, R., Radke, G. A., and Roche, T. E. (1991) *J. Biol. Chem.* **266,** 24650–24656
8. Stoops, J. K., Baker, T. S., Schroeter, J. P., Kolodziej, S. J., Niu, X.-D., and Reed, L. J. (1992) *J. Biol. Chem.* **267,** 14769–14775
9. DeRosier, D. J., Oliver, R. M., and Reed, L. J. (1971) *Proc. Natl. Acad. Sci. U. S. A.* **68,** 1135–1137
10. Fuller, C. C., Reed, L. J., Oliver, R. M., and Hackert, M. L. (1979) *Biochem. Biophys. Res. Commun.* **90,** 431–438
11. Mattevi, A., Obmoloua, G., Schulze, E., Kalk, K. H., Westphal, A. H., deKok, A., and Hol, W. G. J. (1992) *Science* **255,** 1544–1550
12. Maeng, C.-Y., Yazdi, M. A., Niu, X.-D., Lee, H. Y., and Reed, L. J. (1994) *Biochemistry* **33,** 13801–13807
13. Gopalakrishnan, S., Rahmatullah, M., Radke, G. A., Powers-Greenwood, S., and Roche, T. E., (1989) *Biochem. Biophys. Res. Commun.* **160,** 715–721
14. Neagle, J. C., and Lindsay, J. G. (1991) *Biochem. J.* **278,** 423–427
15. Sanderson, S. J., Miller, C., and Lindsay, J. G. (1996) *Eur. J. Biochem.* **236,** 68–77
16. Yang, H., Hainfeld, J. F., Wall, J. S., and Frey, P. A. (1985) *J. Biol. Chem.* **260,** 16049–16051
17. Yang, H., Frey, P. A., Hainfeld, J. F., and Wall, J. S. (1986) *Biophys. J.* **49,** 56–58
18. Maeng, C.-Y., Yazdi, M. A., and Reed, L. J. (1996) *Biochemistry* **35,** 5879–5882
19. Baker, T. S., and Cheng, R. H. (1996) *J. Struct. Biol.* **116,** 120–130
20. Fuller, S. D., Butcher, S. J., Cheng, R. H., and Baker, T. S. (1996) *J. Struct. Biol.* **116,** 48–55
21. Cheng, R. H., Reddy, V., Olson, N. H., Fisher, A., Baker, T. S., and Johnson, E. (1994) *Structure (Lond.)* **2,** 271–282
22. Cheng, R. H., Kuhn, R. J., Olson, N. H., Rossman, M. G., Choi, H.-K., Smith, T. J., and Baker, T. S. (1995) *Cell* **80,** 621–630
23. Belnap, D. M., Groehulski, W. D., Olson, N. H., and Baker, T. S. (1993) *Ultramicroscopy* **48,** 347–358
24. Schroeter, J. P., and Bretaudiere, J.-P. (1996) *J. Struct. Biol.* **109,** 235–247
25. Schierbeek, A. J., Swarte, M. B. A., Dijkstra, B. W., Vriend, G., Reed, R. J., Hol, W. G. J., Drenth, J., and Betzel, C. (1989) *J. Mol. Biol.* **206,** 365–379
26. Koetzle, T. F., and Weng, J. (1987) in *Crystallographic Databases-Information Content, Software Systems, Scientific Applications* (Allen, F. M., Bergerhoff, G., and Sievers, R., eds) pp. 107–132, Data Commission of the International Union of Crystallography, Boun/Cambridge/Chester
27. Takenaka, A., Kizawa, K., Hata, T., Sato, S., Misaka, E., Tamura, C., and Sasada, Y. (1988) *J. Biochem. (Tokyo)* **103,** 463–469
28. Frank, J., Verschoor, A., and Boublick, M. (1981) *Science* **214,** 1353–1355
29. Beale, E. M. L. (1988) *Introduction to Optimization*, pp. 26–29, Wiley-Interscience, New York
30. Gonzalez, R. C., and Wintz, P. (1987) *Digital Image Processing*, 2nd Ed., pp. 425–427, Addison-Wesley, Reading, MA
31. Hessler, D., Young, S. J., Carragher, B., Martone, M., Hinshaw, J., Milligan, R., Masliah, E., Whittaker, M., Lamont, S., and Ellisman, M. (1992) in *Microscopy: The Key Research Tool* (Lyman, C. E., Peachey, L. D., and Fisher, R. M., eds) pp. 73–82, EMSA, Milwaukee
32. Mande, S. S., Sarfaty, S., Allen, M. D., Perham, R. N., and Hol, W. G. J. (1996) *Structure (Lond.)* **4,** 277–286
33. Cheng, R. H. (1992) *Proc. Elec. Microsc. Soc. Amer.* **50,** 996
34. Ladenstein, R., Scheider, M., Huber, R., Bartunik, H.-D., Wilson, K., Schott, K., and Bacher, A. (1988) *J. Mol. Biol.* **203,** 1045–1070